Influence of the adjustable EMBr on the asymmetric flow in a thin slab caster with a misaligned SEN

Influence of the adjustable EMBr on the asymmetric flow in a thin slab caster with a misaligned SEN

A Vakhrushev[1], E Karimi-Sibaki[1], M Wu[2], A Ludwig[2], G Nitzl[3], Y Tang[4], G Hackl[4], J Watzinger[5], A Kharicha[1]

[1]Christian-Doppler Lab for Metallurgical Applications of Magnetohydrodynamics, University of Leoben, Franz-Josef-Str. 18, 8700 Leoben, Austria
[2]Chair of Simulation and Modeling of Metallurgical Processes, University of Leoben, Franz-Josef-Str. 18, 8700 Leoben, Austria
[3]RHI Magnesita GmbH, Kranichberggasse 6, 1120, Vienna, Austria
[4]RHI Magnesita GmbH, Technolgy Centre, Magnesitstrasse 2, 8700, Leoben, Austria
[5]Primetals Technologies, Turmstrasse 44, 4031, Linz, Austria

E-mail: abdellah.kharicha@unileoben.ac.at

Abstract. The thin slab casting (TSC) of steel is a type of the continuous casting (CC) with a narrow funnel-shaped mold, characterized by the rapid solidification and fast production rates. A highly turbulent flow impacts on a growing solid shell due to the constant feeding of the fresh hot melt. That strongly affects the solidification profiles and final quality of the TSC slabs. The presented work numerically investigates the solidification inside the TSC mold with the asymmetric flow pattern caused by the misalignment (tilting) of the submerged entry nozzle (SEN). These effects were considered with and without the applied electromagnetic brake (EMBr). The influence of the adjustable EMBr on the asymmetric flow and solidification profiles including turbulent and magnetohydrodynamic (MHD) effects were studied. During consistent series of simulations, the EMBr was varied between the magnetic poles and the time-averaged velocity and temperature fields were collected. The results showed that symmetric EMBr of a local type could partially improve the asymmetry. An optimal braking scenario was found for the casing speed of 5.5 m/min and maximum EMBr value of 180 mT. The solidification and MHD models including turbulence were developed using OpenFOAM®.

1. Introduction

The thin slab casting (TSC) is known by the close to the net-shape profile, causing a strong turbulence generated in a funnel type mold. The turbulent jets come into the strong interaction with the solidifying shell after they are fed through the submerged entry nozzle (SEN) [1–3]. Thus, the impinging hot melt influences the mushy zone development and due to the partial remelting of the solid shell enhances the breakout risks [4–6]. To control the mold flow an efficient technique was developed through last decades by applying the magnetic field in the form of the electromagnetic braking (EMBr) [7].

The consideration of the Lorentz force in the EMBr-related research is typically limited to the flow damping effects. However, a series of recent studies has revealed the details of its complex topology, which leads to the entrainment of the quiescent melt into the formation of the reverse zones near the jets and in the upper region of the CC mold [8–10].

The flow pattern in the mold, the superheat distribution and the melt solidification are significantly altered under the EMBr during the continuous casting (CC) process [11–17].
The influence of the applied magnetic field on the asymmetric flow inside a TSC mold due to the partial SEN blockage was recently presented by the authors including effects on the solidification profiles [18]. The SEN clogging can occur during deposition of the non-metallic inclusions [19,20] or due to the combined effect with the parasitic solidification inside the SEN bore because of the heat losses [21,22]. A large eddy simulation was performed to investigate the transient asymmetric fluid flow, solidification, and inclusion transport in a slab CC under different EMBr power by Lu et al. [23].
The initial misalignment of the SEN, mechanical distortions due to the thermal expansion of the CC tundish or during the SEN ramping are known to be common issues in the TSC process. The presented work numerically investigates the solidification inside the TSC mold with the asymmetric flow pattern caused by the tilting of the SEN. These effects are considered with and without the applied EMBr.
A previously developed model is applied to simulate the turbulent flow including solidification [24]. The magnetohydrodynamic (MHD) effects are incorporated by using the electric potential method [25]. The influence of the adjustable EMBr on the asymmetric flow and solidification profiles is studied by varying the peak values between the magnetic poles. The time-averaged velocity and temperature fields are collected to define the optimal braking strategy.

2. Numerical model

A mixture volume averaging was used to model the turbulent melt flow accounting for the solidification and the MHD forces. The previously verified mixture approach [24] shows a high performance to model a complex real-size CC process. The corresponding momentum equation of the developed model is:

$$\rho\left[\frac{\partial \vec{u}}{\partial t} + \nabla \bullet (\vec{u} \otimes \vec{u})\right] = \nabla \bullet [\mathrm{dev}(\boldsymbol{\sigma}_{\mathrm{tot}}) - p\mathbf{I}] + \vec{F}_{\mathrm{mush}} + \vec{F}_{\mathrm{MHD}}\,, \tag{1}$$

where the stress $\boldsymbol{\sigma}_{\mathrm{tot}}$ includes molecular viscous forces and the turbulent stress. The large eddy simulation (LES) method was applied using the wall-adapting local eddy-viscosity (WALE) sub-grid scale (SGS) model [26]. The Darcy force $\vec{F}_{\mathrm{mush}}$ represents the drag between the mushy zone and the liquid melt [24]. The Lorentz force $\vec{F}_{\mathrm{MHD}}$ is calculated using the electric potential method [25]. The MHD model implementation can be found elsewhere [8,10]. A conservative formulation was used for the induced electric current density and for the Lorentz force, derived by Ni et al. [27].
The evolution of the temperature field *T* is obtained by solving corresponding energy equation [24]:

$$\rho C_{\mathrm{p}}\left[\frac{\partial T}{\partial t} + \nabla \bullet (\vec{u}T)\right] = \nabla \bullet \lambda \nabla T + \rho L\left[\frac{\partial f_{\mathrm{s}}}{\partial t} + \nabla \bullet (f_{\mathrm{s}} \cdot \vec{u}_{\mathrm{s}})\right], \tag{2}$$

with the specific heat C_{p}, latent heat L and solid fraction f_{s}. The distribution of the solid velocities $\vec{u}_{\mathrm{s}}$ follows the TSC funnel shape [24,28], defining the advection of the released latent heat [3]. The numerical model was implemented in the OpenFOAM® finite volume method (FVM) framework [29].

Table 1. Material properties and casting parameters of the low carbon DD11 steel.

Properties	Symbols	Units	Quantities
Density	ρ	$\mathrm{kg \cdot m^{-3}}$	7850
Specific heat	C_{p}	$\mathrm{J \cdot kg^{-1} \cdot K^{-1}}$	838.2
Thermal conductivity	λ	$\mathrm{W \cdot m^{-1} \cdot K^{-1}}$	35
Liquid dynamic viscosity	μ_{ℓ}	Pa· s	0.0061
Latent heat of fusion	L	$\mathrm{J \cdot kg^{-1}}$	243000
Casting velocity	$\vec{u}_{\mathrm{pull}}$	m/min	5.5
Solidus / liquidus temperature	T_{sol} / T_{liq}	K	1788.15 / 1805.15
Casting temperature	T_{cast}	K	1833.15

The detailed alloy properties calculated using a thermodynamic-kinetic software package IDS [30], casting temperature and pulling velocity are gathered in table 1. The simulation domain overlay is presented in figure 1-a. It includes a funnel-type TSC mold, a strand part, and a SEN; all corresponding dimensions, such as mold width and height, simulated strand length, are marked in figure 1-a for the 100 mm thick slab. The schematics of the SEN tilting is displayed in figure 1-b: the nozzle deviates from the mold symmetry line by an angle $\alpha = 2°$ in the wide face plane. The temperature dependent solid fraction curve is plotted in figure 1-c.

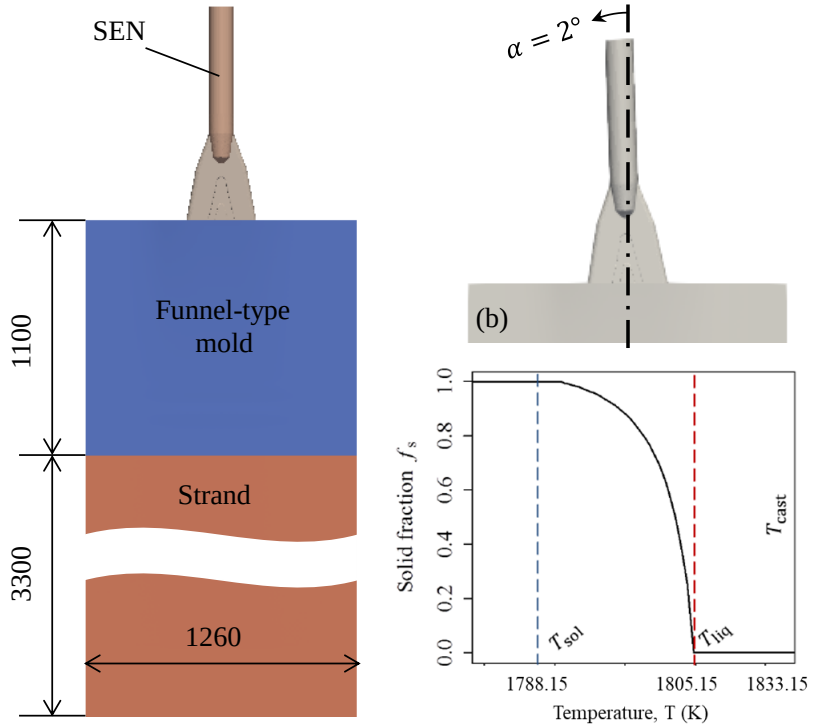

Figure 1. Setting for the TSC modelling: (a) domain outline; (b) schematics of the SEN tilting in the wide face plane; (c) temperature dependent solid fraction curve.

A mold heat flux, which is commonly taken from literature, evaluated from the plant measurements or modeled directly [24,31–33], is defined along the casting direction as a boundary condition in correspondence to figure 2 in Vakhrushev et al. [18]. The secondary cooling zone is described by an effective HTC of 1100 W/m^{2}K, obtained by solving the inverse conduction problem [34].

3. Simulation results

The presented numerical simulations of the melt flow and solidification inside the TSC mold with the tilted SEN (see figure 1-b) were performed according to the following scenarios: (i) without applied magnetic field; (ii) under the symmetric double-pole EMBr of 180 mT; (iii) with the varied EMBr by reducing its power for the left or right pole. The corresponding magnetic field distribution is in figure 2. The direction of the SEN tilting is marked by an arrow. The left brake corresponds to the case, when the maximum EMBr power is on the left side of the mold, as shown in figure 2-b. The similar principle applies for the scenario with the right-side brake in figure 2-c. The percentage marks the amount of the magnetic field reduction on the opposite site. The peak value is 180 mT for all scenarios.

The simulation results for the non-EMBr case and for the symmetric braking are detailed in figure 3. The time-averaged velocity field and temperature distribution were collected during the modelling for the comparison. Velocity magnitude in figure 3-a shows, that without magnetic field the jet on the right side of the mold (tilting-wise direction) goes deeper into the melt pool. The flow stagnation zone is

formed at the meniscus region. On the left side the upper roll remains close to the top surface. That results in the colder region on the right side in figure 3-c with more superheat transported to the left.

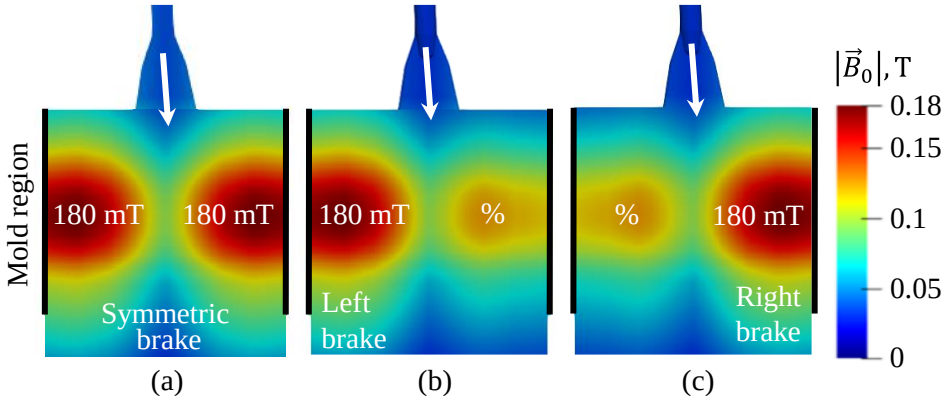

Figure 2. Distribution of the applied magnetic field for the cases (a) with the symmetric EMBr; adjustable braking with the peak value (b) on the left and (c) on the right side.

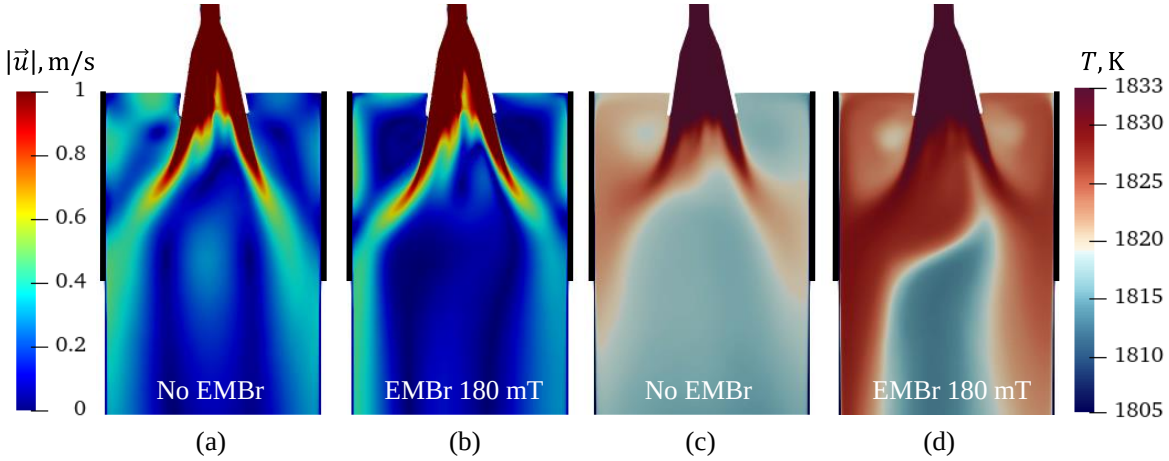

Figure 3. Time-averaged velocity magnitude for (a) non-EMBr case and (b) with the EMB; time-averaged temperature field (c) without and (d) under the applied magnetic field.

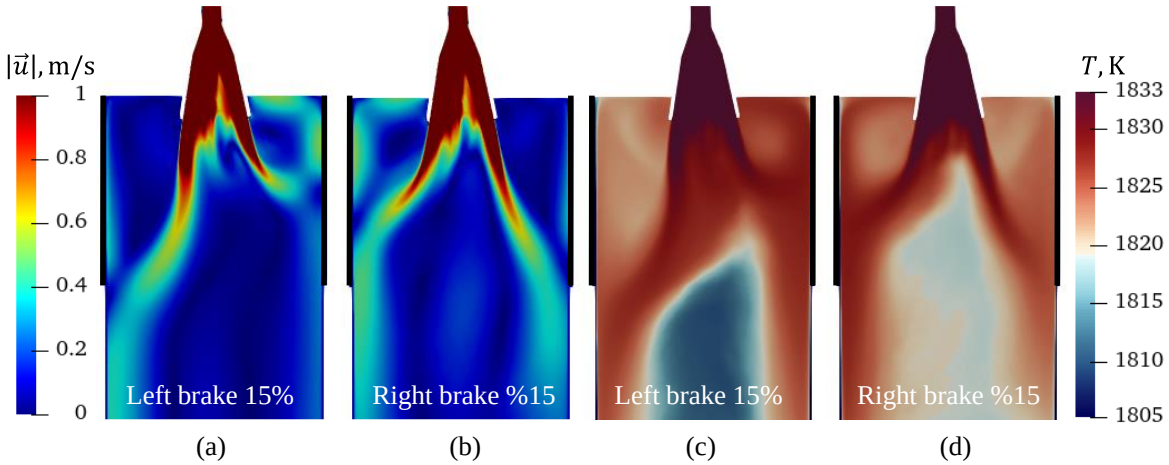

Figure 4. Time-averaged velocity distribution with the 15% more braking (a) on the left and (b) right side; time-averaged temperature field for the corresponding (c) left and (d) right 15% brake.

When the EMBr of 180 mT is applied the flow becomes more symmetric with a slightly slower upper roll on the right in figure 3-b. The uniformity of the temperature field in figure 3-d is improved as well. However, more superheat is brought to the narrow walls with a colder melt zone formed in the center.
Next, the adjustable EMBr technique was applied and analyzed by varying the magnetic field between the poles by 15% of its maximum value of 180 mT. It should be reminded for the readers, that a linear variation of the EMBr power causes a quadratic change of the Lorentz force [10]. Thereby, a change of the applied magnetic field by 15% results in 32.2% for the acting MHD force.
The modelling results in figure 4 distinctively show, that a jet goes deeper on the dominant EMBr side. The superheat transport shifts correspondingly towards the opposite side with a weaker magnetic field.

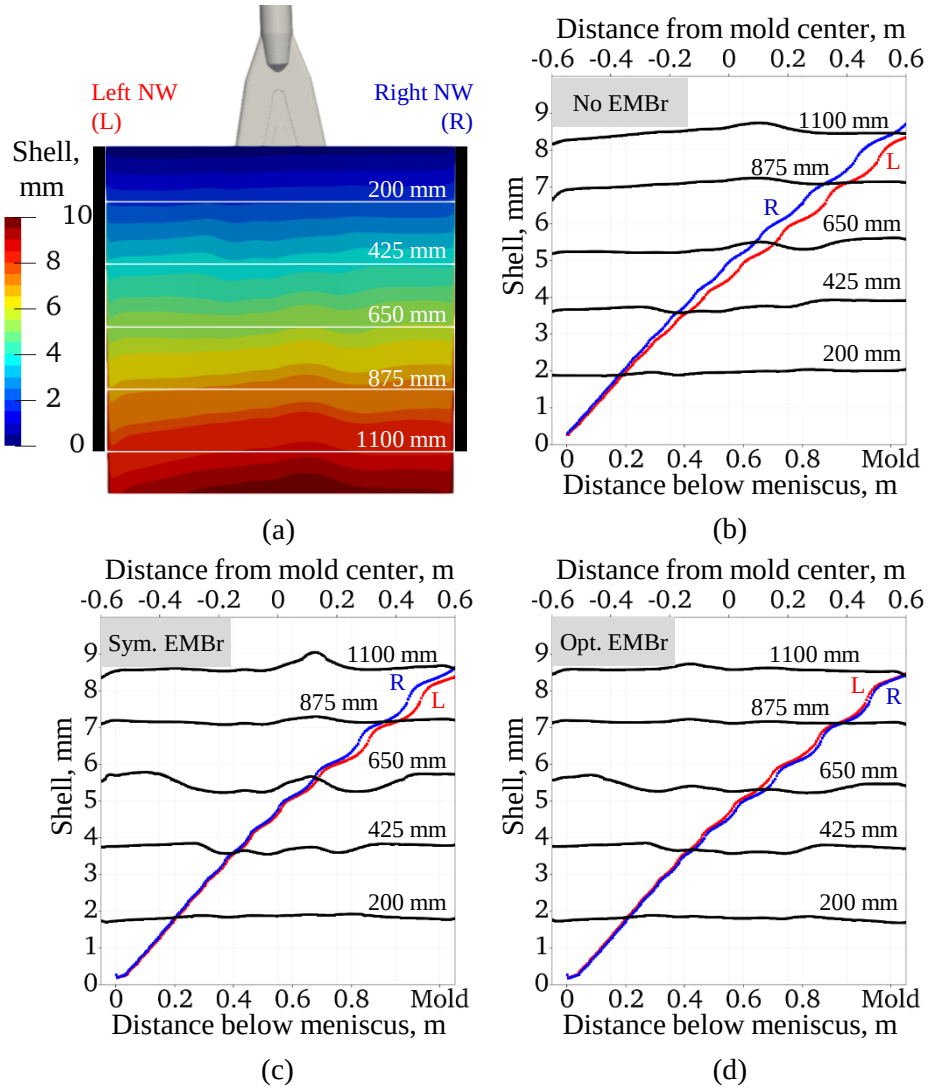

Figure 5. Adjustable EMBr simulation results: (a) shell thickness (front wide face) for the non-EMBr case; shell thickness profiles along the narrow sides and at the transversal lines for the scenarios (b) without magnetic field; (c) symmetric brake (180 mT); (d) optimized EMBr with 4% more power on the left side.

The simulations of the symmetric EMBr showed, that the application of the magnetic field leads itself to the improvements in the flow pattern with a slightly slower upper roll (figure 3-b) and colder region

(figure 3-d) on the right side of the domain. Applying this knowledge along with the conclusions for the 15% left and right brake in figure 4, the optimal brake of 4% more power on the left side was consequently found through the manual simulation series.
The centerlines of the left and the right narrow sides are marked in figure 5-a with the red L and blue R letters and text respectively. They are specified for solid shell profiles along the casting direction. The transversal thickness is analyzed along the horizontal lines, which are at 200 mm, 425 mm, 650 mm, 875 mm, and 1100 mm (mold exit) below the meniscus in figure 5-a. Vertical and horizontal shell thickness profiles are presented on the corresponding subplots of figure 5.
Figure 5-a shows the distribution of the solid shell thickness across the front wide face of the TSC mold for the non-EMBr case. The remelting on the left and a thicker shell on the right are detected. Such an asymmetry can cause the mechanical stresses, tearing of the solid shell and leads to the costly breakout. The significant deviations, especially at the mold exit, are detected on the narrow sides in figure 5-b.
The uniform magnetic field improves shell thickness on the narrow sides in figure 5-c: deviation of the shell thickness between left and right is reduced. The solidified shell on the narrow sides in figure 5-c is slightly thinner than in the non-EMBr case in figure 5-b. That is explained by the enhanced superheat transport under magnetic field, if referred to figure 3-d in comparison to figure 3-c. The thickness kinks in the transversal shell profiles in figure 5-c are due to the colder central zone in figure 3-d. The remelting sites correspond to the location of the stabilized jets, that bring a fresh melt.
The resulting shell distribution under the optimized brake scenario (4% more EMBr power on the left) is detailed in figure 5-d. A good fit achieved between the narrow side profiles. The horizontal thickness distribution became more uniform and symmetric. Some insignificant deviations still appear; however, the main issues and the unevenness of the shell thickness are removed. More precise solution and the automation of the adjustable EMBr optimization are the topics for the future research.

4. Conclusions

In the presented work the solidification inside the TSC mold with the asymmetric flow pattern caused by the misalignment (tilting by an angle of 2°) of the SEN was numerically investigated. These effects were considered without and with the applied electromagnetic brake.
The developed solidification and MHD models were used to reveal the influence of the adjustable EMBr on the solid shell growth considering interaction with the asymmetric turbulent flow. The EMBr variation was done by increasing or decreasing the magnetic field between the left and right poles.
During consistent series of simulations, the time-averaged velocity and temperature fields were collected for the different magnetic field settings to perform a comparative study. The results showed that the symmetric EMBr of a local type could partially remove the asymmetry in the flow patter, superheat distribution and solidification. An optimal braking scenario was found for the casing speed of 5.5 m/min and maximum EMBr value of 180 mT by having the magnetic field stronger by 4% on the left side.

5. Acknowledgments

The authors acknowledge the financial support by the Austrian Federal Ministry of Economy, Family and Youth and the National Foundation for Research, Technology and Development within the framework of the Christian Doppler Laboratory for Metallurgical Applications of Magnetohydrodynamics.

References

[1] Wu M, Vakhrushev A, Nummer G, Pfeiler C, Kharicha A and Ludwig A 2010 *TOTPJ* **2** 16–23
[2] Vakhrushev A, Wu M, Ludwig A, Tang Y, Hackl G and Nitzl G 2012 *IOP Conf. Ser.: Mater. Sci. Eng.* **33** 012014
[3] Wu M, Vakhrushev A, Ludwig A and Kharicha A 2016 *IOP Conf. Ser.: Mater. Sci. Eng.* **117** 012045
[4] Iwasaki J and Thomas B G 2012 *Supplemental Proceedings* ed Tms (Hoboken, NJ, USA: John Wiley & Sons, Inc.) pp 355–62

[5] Luk'yanov S I, Suspitsyn E S, Krasilnikov S S and Shvidchenko D V 2015 *Int J Adv Manuf Technol* **79** 1861–8
[6] Zappulla M L S, Cho S and Thomas B G 2019 *Steel Res. Int.* **90** 1800540
[7] Thomas B G and Cho S M 2018 *IOP Conf. Ser.: Mater. Sci. Eng.* **424** 012027
[8] Vakhrushev A, Kharicha A, Liu Z, Wu M, Ludwig A, Nitzl G, Tang Y, Hackl G and Watzinger J 2020 *Metall. Mater. Trans. B* **51** 2811–28
[9] Kharicha A, Vakhrushev A, Karimi-Sibaki E, Wu M and Ludwig A 2021 *Phys. Rev. Fluids* **6** 123701
[10] Vakhrushev A, Kharicha A, Karimi-Sibaki E, Wu M, Ludwig A, Nitzl G, Tang Y, Hackl G, Watzinger J and Eckert S 2021 *Metall. Mater. Trans. B* **52** 3193–207
[11] Ha M Y, Lee H G and Seong S H 2003 *Journal of Materials Processing Technology* 18
[12] Chaudhary R, Thomas B G and Vanka S P 2012 *Metall and Materi Trans B* **43** 532–53
[13] Thomas B G, Singh R, Vanka S P, Timmel K, Eckert S and Gerbeth G 2015 *Journal for Manufacturing Science and Production* **15** 93–104
[14] Vakhrushev A, Kharicha A, Liu Z, Wu M, Ludwig A, Nitzl G, Tang Y, Hackl G and Watzinger J 2019 *The 8th International SteelSim Conference* SteelSim 2019 (AIST) pp 615–9
[15] Garcia-Hernandez S, Gonzalez-Guzman C H, Morales Davila R, Barreto J de J, Gutierrez E and Calderon-Ramos I 2020 *Crystals* **10** 958
[16] Vakhrushev A, Kharicha A, Wu M, Ludwig A, Nitzl G, Tang Y, Hackl G, Watzinger J and Rodrigues C M G 2020 *IOP Conf. Ser.: Mater. Sci. Eng.* **861** 012015
[17] Wang C, Liu Z and Li B 2021 *Metals* **11** 948
[18] Vakhrushev A, Kharicha A, Karimi-Sibaki E, Wu M, Ludwig A, Nitzl G, Tang Y, Hackl G and Watzinger J 2022 *steel research int.* **93** 2200088
[19] Barati H, Wu M, Kharicha A and Ludwig A 2018 *Powder Technology* **329** 181–98
[20] Barati H, Wu M, Michelic S, Ilie S, Kharicha A, Ludwig A and Kang Y-B 2021 *Metall Mater Trans B* **52** 4167–78
[21] Barati H, Wu M, Kharicha A and Ludwig A 2020 *Steel Res. Int.* **91** 2000230
[22] Vakhrushev A, Kharicha A, Wu M, Ludwig A, Tang Y, Hackl G, Nitzl G, Watzinger J and Bohacek J 2021 *Metals* **11** 1375
[23] Lu H, Zhong Y, Ren W, Ren Z and Lei Z 2022 *steel research int.* **93** 2200518
[24] Vakhrushev A, Wu M, Ludwig A, Tang Y, Hackl G and Nitzl G 2014 *Metall. Mater. Trans. B* **45** 1024–37
[25] Davidson P A 2001 *An Introduction to Magnetohydrodynamics* (Cambridge University Press)
[26] Nicoud F and Ducros F 1999 *Flow, Turbulence and Combustion* **62** 183–200
[27] Ni M-J, Munipalli R, Huang P, Morley N B and Abdou M A 2007 *Journal of Computational Physics* **227** 205–28
[28] Vakhrushev A, Kharicha A, Wu M, Ludwig A, Nitzl G, Tang Y, Hackl G, Watzinger J and Rodrigues C M G 2022 *J. Iron Steel Res. Int.* **29** 88–102
[29] Weller H G, Tabor G, Jasak H and Fureby C 1998 *Comput. Phys.* **12** 620
[30] Miettinen J, Somani M, Visuri V-V, Koskenniska S, Louhenkilpi S, Fabritius T and Kömi J 2022 *steel research int.* srin.202200120
[31] Camporredondo S. J E, Castillejos E. A H, Acosta G. F A, Gutiérrez M. E P and Herrera G. M A 2004 *Metall. Mater. Trans. B* **35** 541–60
[32] Zhang H and Wang W 2017 *Metall. Mater. Trans. B* **48** 779–93
[33] Niu Z, Cai Z and Zhu M 2020 *Ironmaking & Steelmaking* **47** 1135–47
[34] Bohacek J, Kominek J, Vakhrushev A, Karimi-Sibaki E and Lee T-W 2021 *OpenFOAM Journal* **1** 27–46